| RESEARCH ARTICLE

Elevating Red and Near-Infrared Detectivity With CsSnI$_3$ Perovskite Photodetectors Featuring GO and PCBM as Charge Transport Layers

Pallavi Pandey 🔾 | Akhilesh Kumar Chaudhary 🔾 | Sudhanshu Verma 🔾

Department of Electronics and Communication Engineering, Madan Mohan Malaviya University of Technology, Gorakhpur, Uttar Pradesh, India

Correspondence: Sudhanshu Verma (svermaeced@gmail.com)

ABSTRACT

This study focuses on enhancing the performance of photodetector through the utilization of inorganic perovskite material. It emphasizes that the unique properties of perovskite materials contribute to the superior performance of the photodetector. The focus is on the design and enhancement of CsSnI$_3$-based photodetector having graphene oxide (GO) and PCBM as charge transport layer, analysing their potential for improved operation. The design process involves a series of optimizations to the device layers, particularly the absorber layer's thickness and defects, which is critical for enhanced efficiency. The designed photodetector exhibits a better responsivity and detectivity in red and near infrared region and maximum responsivity of 0.68 A/W and detectivity of 9×10^{12} Jones. The SCAPS-1D tool is employed to facilitate the design analysis, enabling the fine-tuning of the device parameters. The findings highlight the effectiveness of perovskite materials in boosting photodetector performance.

1 | Introduction

Photodetectors possess the ability to directly transform light energy into electrical signals, holding a distinct level of importance within the fields of photonics and electronics. They have garnered considerable interest and found utility in diverse domains such as industrial manufacturing, military operations, biochemical analysis, optical communication and scientific investigation [1–3]. Typically, photodetectors are classified into two main types: wavelength-specific detectors (such as ultraviolet, visible and infrared detectors) and broadband detectors. The performance of photodetectors is determined by several critical parameters, namely wavelength range, responsivity, detectivity, noise and dynamic range. Significant advancements have been achieved in improving the figure of merit for photodetectors through various research and development initiatives [4]. Despite these advancements, photodetector technology faces persistence challenges

that limit its performance and adoption. Infrared detectors are expensive and non-uniform, hindering their large-scale application. Many IR detectors require cryogenic temperatures, making them complex and sensitive to temperature fluctuations. Although nanostructured photodetectors offer ultrafast response times, they may compromise sensitivity; thin films and heterostructures also exhibit faster responses but lower sensitivity. Graphene's low absorption rate in visible light necessitates the use of composite materials to enhance photoresponse and external quantum efficiency. Scalability and production issues, especially for flexible photodetectors, further hinder commercial viability. Additionally, precise control over fabrication parameters is crucial for optimizing device performance and reliability. Despite advancement, improving the responsivity and detectivity of photodetectors remains essential for application demanding high light sensitivity [5]. In recent decades, solution-processed photodetectors have been developed using low-cost semiconductors

materials [6–8]. Many of these photodetectors have demonstrated commendable reaction rates and detectivity comparable to that of conventional semiconductors such as silicon and InGaAs [9], which are produced using relatively expensive vacuum-deposition techniques. Among the emerging materials, hybrid perovskite-based photodetectors are gaining attention for their outstanding semiconducting properties in recent research work. The hybrid perovskite compound having structure of ABX_3 consist of a monovalent cation (A) such as $CH_3NH_3^+$ (MA), $NH_2CHNH_2^+$ (FA) or Cs^+, a divalent metal cation (B) such as Pb^{2+} or Sn^{2+} and a halide anion (X) such as Cl^-, Br^- or I^- [10–13], including high light-absorbing capability and excellent charge carrier mobility [14]. Furthermore, the straightforward processing of perovskites, combined with their structural versatility, holds promising prospects for various applications. Despite the substantial advancements achieved during the manufacturing process of hybrid lead halide active materials, there persist certain scientific hurdles and environmental barriers hindering the potential for commercial utilization. Among these challenges, the detrimental impact of lead toxicity stands out as a significant limitation associated with the application of hybrid lead halide perovskite [14, 15]. Thus, there is a critical need to develop and introduce lead-free perovskite alternatives that enhance performance characteristics, making them suitable for integration into photodetectors. In comparison to organic–inorganic metal halide perovskites, all-inorganic tin-based perovskite may offer the advantage of improved thermal stability though preserving advantageous optoelectronics characteristics for PV application. $CsSnI_3$ exhibits characteristics typical of a p-type semiconductor, including notable hole mobility, a desirable band gap of approximately 1.3 eV, minimal exciton binding energy and significant photosensitive absorption [16–19]. Chen et al. [20] demonstrated a perovskite photodiode with graphene electrodes, reporting a responsivity (R) of 22 mA/W and detectivity of 3.55×10^9 Jones. Similarly, Zibo et al. [21] constructed a photodiode using WS_2/metal halide perovskite, attributing the enhanced photoresponse to the inclusion of perovskite in WS_2. Atomic force microscopy (AFM) was employed to visualize both of the photoelectric and dark current generated at the interface junction. They conclude that charge dissociation and transport at the WS_2-perovskite interface governed by interfacial properties. Zhou et al. [22] developed a perovskite photodiode with an R value of approximately 198 mA/W. Jiangyoung et al. [23] successfully fabricated a photodiode based on perovskite material $CsCu_2I_3$ architecture. They thoroughly investigated its operational mechanism using energy band diagrams. Notably, the device demonstrated a detectivity of 3.45×10^{11} Jones. Building on these developments, this work optimizes photodetector performance by using a multilayered structure with $CsSnI_3$ as the absorber layer chosen for its stability under varying environmental conditions, including humidity and temperature. The stability of $CsSnI_3$ can be enhanced by stabilizing agents, such as ascorbic acid, which prevents the oxidation of Sn^{2+} to Sn^{4+}, preserving the material's structure and optoelectronic properties even in humid conditions. Studies show that optimizing phase stability and defect passivation is crucial to enhance performance under temperature fluctuations [24]. This structure also incorporates PCBM and graphene oxide (GO) as the electron and hole transport layers, respectively, with nickel (Ni) and fluorine-doped tin oxide (FTO) serving as the electrodes. This design is intended to improve the optoelectronic properties of the photodetector through enhanced structural and interfacial properties, setting the stage for next-generation photodetectors.

2 | Numerical Simulations Using SCAPS 1D

In this work, numerical simulations of the proposed perovskite photodetector (PPD) are conducted using the SCAPS-1D software, also known as Solar Cell Capacitance Simulator. SCAPS-1D is renowned for its accuracy in modelling photovoltaic characteristics in thin-film devices and is employed to analyse the performance of the PPD. The architecture of this device includes a perovskite absorber layer flanked by charge transport layers, which significantly affect the device's efficiency. The simulations are based on differential equations, including the Poisson equation, carrier continuity equations and drift-diffusion equations. The Poisson equation, in particular, describes the relationship between the electric field (E) in a perovskite/n-type semiconductor junction and the space charge density (ρ) [25, 26].
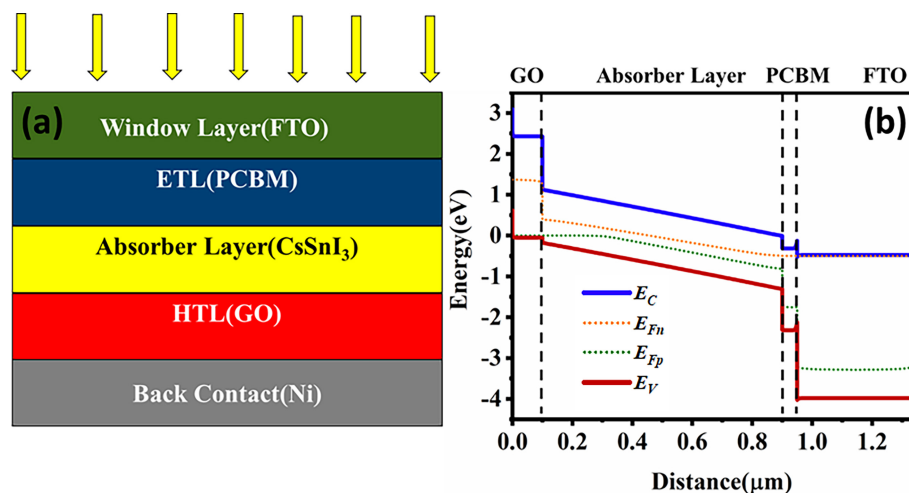

FIGURE 1 | (a) Structured layers in perovskite photodetectors, (b) perovskite-based photodetector energy band diagram.

$$\frac{d}{dx}\left(\varepsilon(x)\frac{d\psi}{dx}\right) = q\left[p(x) - n(x) + N_D^+(x) + N_A^-(x) + p_t(x) - n_t(x)\right] \tag{1}$$

$$\frac{i}{j}\frac{dj_p}{dx} + R_p(x) - G(x) = 0 \tag{2}$$

$$-\frac{i}{j}\frac{dj_n}{dx} + R_n(x) - G(x) = 0 \tag{3}$$

Here, the charge of the electron is represented as q, the dielectric constant as ε, the electrostatic potential as ψ, the concentration of electrons as n, the concentration of free holes as p, the density of trapped electrons as n_t, the density of trapped holes as p_t, the ionized shallow uniform donor doping concentration as N_D^+ and the ionized shallow uniform acceptor doping concentration as N_A^-. The rates of recombination of electrons and holes are denoted as $R_n(x)$ and $R_p(x)$, respectively, whereas the rate of generation of charge carriers is represented as $G(x)$. The electron and hole current densities are indicated as j_n and j_p, respectively.

Figure 1a illustrates the stratified schematic configuration of a device based on perovskite, whereas Figure 1b display the energy band diagram of individual layers employed in the device architecture. The transport layers for holes and electrons are composed of GO and PCBM, respectively, with the active layer being comprised of the perovskite material $CsSnI_3$. Functioning as the front electrode is FTO, which serves as transparent conductive oxide layer, while the back electrode is selected as Ni. The parameter values for each component of the device utilize in the perovskite-based photodetector detailed in Table 1. These values have been sourced from prior theoretical and experimental studies [27–29, 30–32]. Furthermore, interface layers PCBM/$CsSnI_3$ and GO/$CsSnI_3$ have been added to investigate the effects of recombination occurring at the interface.

Figure 1b illustrates the energy band diagram of a proposed PPD, highlighting the functions of GO as hole transport layer (HTL) and PCBM as the electron transport layer (ETL). This diagram delineates the relative positions of the valence and conduction bands of each material, providing essential insights into the behaviour of charge carriers, including electron (e^-) and holes (h^+). In operation, when the active layer ($CsSnI_3$) absorbs photons, electron–hole pairs are generated. The electrons have higher energy levels (less negative) than the holes, given their respective positions in the conduction band. The favourable downward energy gradient enables electron to flow easily from the active layer into the PCBM layer, facilitating their transport towards the FTO electrode. Simultaneously, holes in the valence band of the absorber move towards the HTL, with the band alignment encouraging hole movement from the perovskite layer to the GO layer. The GO layer acts as a selective pathway, allowing holes to migrate towards the back electrode while effectively impending electrons because of its higher conduction band minimum (CBM) compared to the active layer CBM. The energy band diagram illustrates a configuration that facilities the separation and targeted transport of charge carriers: electrons efficiently flow to the ETL (PCBM) and onward to the FTO electrode, while holes are directed to the HTL (GO) and ultimately to the back electrode. This charge carrier separation minimizes recombination losses and underpins the enhanced performance of the PPD. The quality of the GO and PCBM interface is a critical factor influencing the charge transport and overall performance of the device. Defects, both at the material level and at the interface, can reduce charge mobility, increase recombination and affect long-term stability. Ensuring high-quality interfaces with minimal defect is key to maximizing the performance of devices using these materials.

3 | Results and Discussion

3.1 | Enhancing the Active Layer Thickness for Optimization

The impact of the active layer thickness in the PPD structure FTO/PCBM/$CsSnI_3$/GO/Ni is investigated by varying the active material thickness from 0.4 to 1.4 µm, while maintaining the

TABLE 1 | Parameters of different layers of the proposed PPD.

Parameters	Unit	FTO	PCBM	$CsSnI_3$	GO
Thickness (d)	(µm)	0.4	0.05	0.8	0.1
Bandgap (E_g)	(eV)	3.5	2	1.3	2.48
Electron affinity (χ)	(eV)	4.3	3.39	3.6	2.3
Dielectric constant (ε)	—	9	4	9.93	10
CB effective DoS (N_c)	cm^{-3}	2.2×10^{18}	1×10^{21}	1×10^{19}	2.2×10^{18}
VB effective DoS (N_v)	cm^{-3}	1.8×10^{19}	2×10^{20}	1×10^{18}	1.8×10^{19}
Electron & hole thermal velocity ($V_{th}(n)$ & $V_{th}(p)$)	cm/s	1×10^{7}	1×10^{7}	1×10^{7}	1×10^{7}
Mobility of electron (μ_e)	cm^{-2}V^{-1}s^{-1}	2×10^{1}	1×10^{-2}	1.5×10^{3}	2.6×10^{1}
Mobility of hole (μ_h)	cm^{-2}V^{-1}s^{-1}	1×10^{1}	1×10^{-2}	5.85×10^{2}	1.23×10^{2}
Donor concentration (N_D)	cm^{-3}	1×10^{18}	1×10^{18}	—	—
Acceptor concentration (N_A)	cm^{-3}	—	—	1×10^{14}	2.5×10^{18}
Defect density (N_t)	cm^{-3}	1×10^{14}	1×10^{14}	1×10^{14}	1×10^{14}

other layer's parameters constant as in Table 1. Initially, the short circuit current density (J_{SC}) exhibited an increase, attributed to enhanced photon absorption. However, beyond a certain thickness J_{SC} plateaued because of recombination effects. A thicker absorber layer initially boosts J_{SC} by absorbing more photons, particularly those with longer wavelengths and higher energy, leading to increased charge carrier (electron and hole) production in the photovoltaic device. As the thickness of the perovskite $CsSnI_3$ layer increased in the devices, the short-circuit current (J_{SC}) displayed a rise and reached a value of 33.6 mA/cm^2 at 0.8 μm. The absorber layer's thickness exhibits different percentage increases when transitioning from 0.6 to 0.8 μm (1.02%) and from 0.8 to 1.0 μm (0.43%). Beyond this point, the thickness increment becomes negligible. Consequently, a thickness of 0.8 μm is considered optimal, as it balances the increase in series resistance. This conclusion is supported by Figure 2b, which illustrates that the power output reaches its maximum at this thickness.

Notably, optimal performance is observed at 0.8 μm, as depicted in Figure 2a,b. This optimal thickness arises from interplay between photon absorption rates and charge carrier recombination. As the active layer thickness, more photons are absorbed, leading to increased recombination rates. Conversely, a thin film enhances carrier extraction at the electrodes. Performance decreases with reduced thickness because of lower photon absorption.

3.2 | Effect of HTL Layer Thickness

The HTL is a critical component in PPDs. It acts as a barrier between the perovskite absorber layer and the back electrode, enabling efficient hole extraction. GO is a popular HTL material because of its high charge mobility and ability to promote exciton dissociation. By incorporating a GO HTL, the short-circuit current density J_{SC} of PPD is significantly improved.

While varying the HTL thickness within the range of 10 to 110 nm can impact series resistance and charge transfer, a thickness of 100 nm is generally preferred as shown in Figure 3. This thickness provides a good balance between these factors, resulting in optimal PPD performance.

3.3 | Effect of ETL Layer Thickness

The ETL is critical component in PPDs. It serves as a bridge between the perovskite absorber layer and the front electrode, enabling efficient electron extraction. PCBM is a popular ETL material because of its high electron mobility and suitable energy band alignment with perovskite. By incorporating a PCBM ETL, the short-circuit current density of the PPD is significantly improved, as it reduces recombination losses and enhances electron transport.

While varying the ETL thickness within the range of 10 to 100 nm has a little effect on the overall PPD performance; however, a thickness of 50 nm is taken as thickness of ETL for next optimization stage. Thickness from 50 to 100 nm can be used without compromising performance as shown Figure 4.
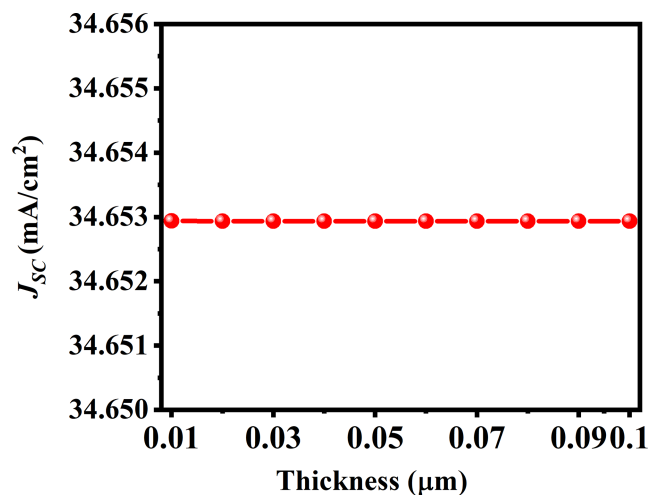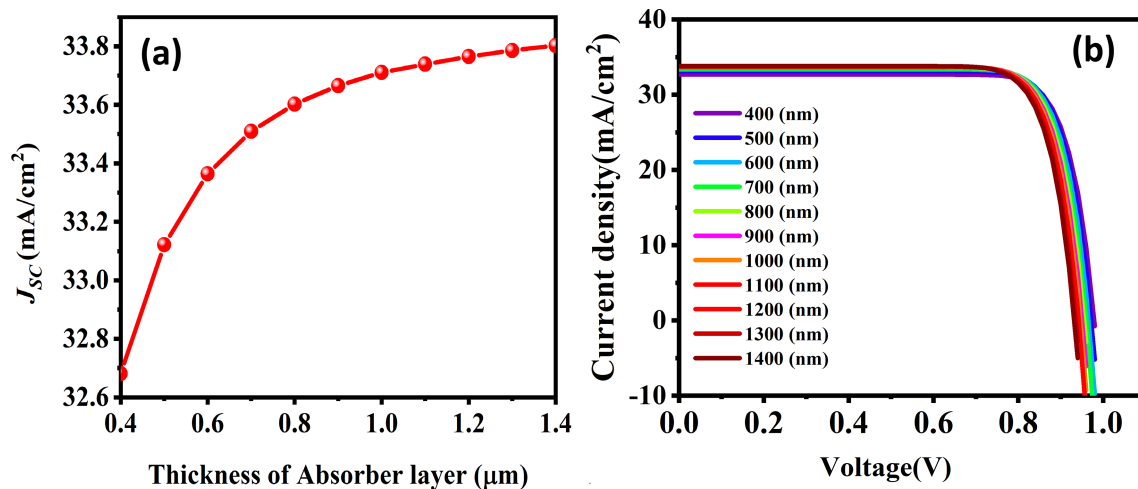
FIGURE 3 | J_{SC} variation with HTL layer thickness.

FIGURE 2 | (a) Variation of J_{SC} with absorber layer thickness in $CsSnI_3$-based photodetector. (b) J-V relationship.
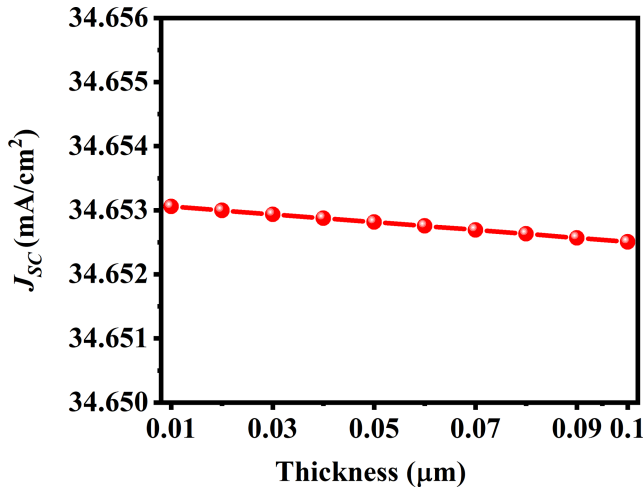
FIGURE 4 | J_{SC} Variation with ETL layer thickness.

FIGURE 5 | Effect of acceptor density on J_{SC} in CsSnI$_3$ absorber layer.

3.4 | The Impact of Varying Concentrations of Dopants on the Absorber Layer

The doping concentration, an essential factor, has a direct impact on various photonic characteristics including recombination rate of carriers and open circuit voltage (V_{OC}), as well as the diffusion length. The carrier concentration is systematically adjusted from 10^9 to 10^{16} cm^{-3} to investigate its impact on the photovoltaic parameters of the device. The goal is to determine the optimal acceptor doping density (N_A) for the absorber layer, while keeping the other parameters of the ETL and HTL constant. The highest current density recorded is 33.36 mA/cm^2, at an acceptor density of 10^{14} cm^{-3}, which is identified as the optimum acceptor density as in Figure 5.

The variations, as reflected in Figure 5, investigates the effect of varying N_A within the absorber layer of the PPD. The purpose of adjusting N_A from 10^9 to 10^{16} cm^{-3} is to determine the optimal doping level that aligns with the doping values of HTL and ETL for a smoother flow of charge carriers after band formation, thus optimizing the performance of the photodetector. Upon reaching an absorber acceptor density of 10^{14} cm^{-3}, the device performance is observed to be at its optimum, as indicated by the maximum J_{SC} value.

However, as N_A continues to increase beyond this point, there is a marked decline in J_{SC}. The steep downward trends after 10^{14} cm^{-3} highlights a reduction in photodetector performance, attributed to increased charge carrier recombination. This recombination diminishes the minority carrier concentration, thereby shortening the diffusion length and decreasing carrier mobility within the device.

3.5 | Influence of the Defect Density (N_t) Within the Active Layer

The performance of the PPD is significantly impacted by the quality and structure of the absorber layer, as well as the defect density at the interface of this layer. During operation, when light in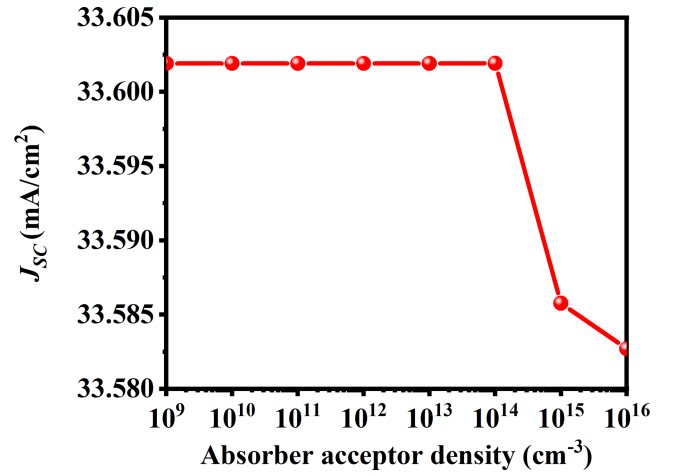teracts with the device, electron–hole pairs are generated within the absorber layer. However, defects arising from suboptimal fabrication processes can increase the defect density, leading to enhanced rates of carrier recombination that detrimentally affect the performance [28, 33]. These defects include point defects, which are deviations in the arrangement of constituent atoms and can manifest as Frenkel or Schottky defects. Furthermore, grain boundaries and dislocations also contribute to the overall defect landscape within the solid [34]. To quantify the influence of these defects on the PPD, the Shockley–Read–Hall (SRH) recombination model is applied, providing insights into how defect densities correlate with the device's functional parameters [35].

$$R^{SRH} = \frac{np - n_i^2}{\tau_n \left(p + N_V e^{\left(\frac{E_t}{KT} \right)} \right) + \tau_P \left(n + N_C e^{\left(E_g - \frac{E_t}{KT} \right)} \right)} \quad (4)$$

Considering the concentrations of mobile charge carriers, represented as p and n respectively, alongside factors such as energy level (E_t), trap defect concentration (N_t) and intrinsic concentration (n_i) is crucial. Analysis of Equation (4) reveals that the inclusion of defect density (N_t) within the perovskite layer significantly influences the lifetime τ and diffusion length (L) of the charge carriers are described by the following equations.

$$\tau = \frac{1}{\sigma \times N_t \times V_{th}} \quad (5)$$

The symbol σ denotes the carriers of the capture cross section, τ signifies the duration of charge carriers' life, V_{th} denotes the thermal velocity of charge carriers and N_t represents the defect density within the perovskite layer [36].

The expression for the diffusion length is

$$L = \sqrt{D_\tau} \quad (6)$$

where D represents diffusion coefficient, and by utilizing Equation (5), we can analyse

5 of 11

$$D = \frac{\mu \times T \times k_g}{q} \tag{7}$$

The symbol k_g denotes the Boltzmann constant, whereas T represents the temperature, q signifies the electron's charge and μ represents the charge carrier's mobility.

Simulated results illustrating the impact of defect density variations in the absorber layer on the device's performance has been identified as 1×10^{14} cm^{-3} (Figure 6).

3.6 | Analysis of Defect Density at the Interface

This section examines the relationship between the interface defect densities and device parameters. The defect densities observed at the GO/CsSnI$_3$ and CsSnI$_3$/PCBM interface defects ranged from 10^{10} to 10^{16} cm^{-2}.

Once the defect density surpasses 10^{14} cm^{-2}, a slight degradation in J_{SC} is evident, as illustrated in Figure 7a,b. In the case of GO/CsSnI$_3$ junction, J_{SC} remains relatively stable up to 10^{14} cm^{-2}, after which it sharply decreases (Figure 5a).
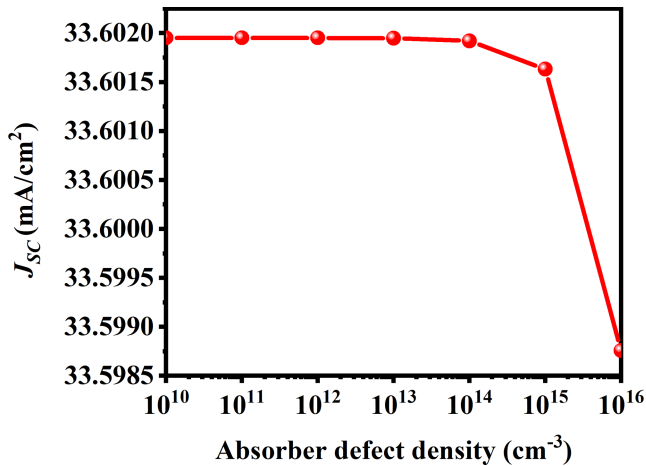

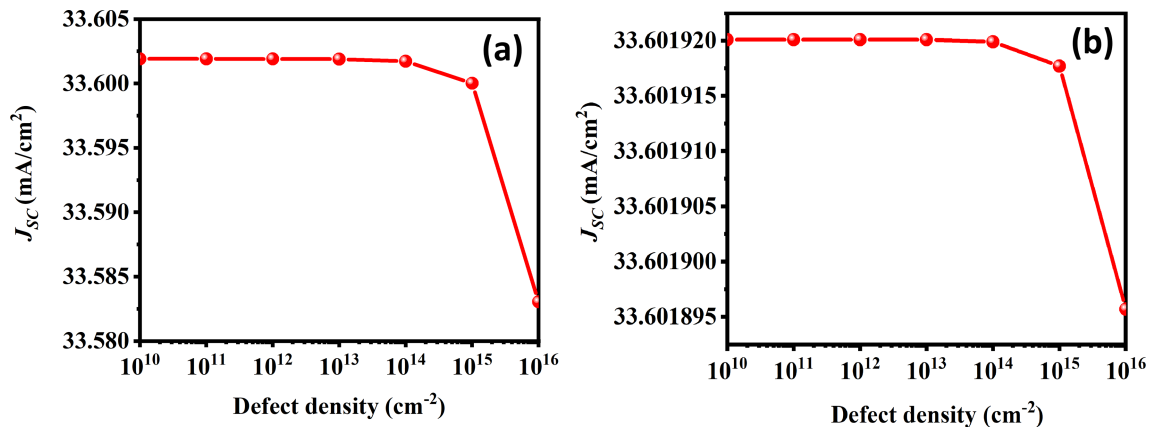**FIGURE 6** | Variation of J_{SC} relative defect density in CsSnI$_3$ absorber layer.

The significant decline in device performance is identified as being caused by a large increase in trap states acting as recombination centres, which occurs as interface defect densities increase [34, 35–37].

3.7 | Temperature Analysis

The performance of the optoelectronic device is significantly impacted when the device is exposed to higher ambient temperature. Variation in climates and weather condition across different regions globally can influence the functionality of optoelectronic devices. Consequently, elevated temperatures may pose challenges to the accuracy of the photodetector. In the current simulations, we explore the influence of ambient temperature, ranging from 300 to 450 K, on the performance of the proposed PPD. As elucidated in Figure 8a, J_{SC} exhibits an increase with the rise in ambient temperature.

This increment is principally because of the contribution of thermally generated current alongside the photogenerated current, maintained under a constant intensity and power of incident light.

Simultaneously, it is observed that V_{OC} reduces as the temperature climbs (Figure 8b). Ideally, a higher V_{OC} is preferable as it reflects a more effective charge separation. The thermal excitation of charge carriers at higher temperatures leads to enhanced recombination activities, thereby lowering V_{OC}. Consequently, for the PPD to achieve superior detection accuracy, it is advantageous to operate at a lower thermal current, which is at lower ambient temperatures.

Several important factors can be used to represent the relationship between a photodetector's temperature (T) and short-circuit current density (J_{SC}). Bandgap energy and recombination rates are primary temperature-dependent factors that affect J_{SC}.

In general, J_{SC} can be estimated to rise marginally with temperature. The following is an expression for a simplified relationship [38]:

$$J_{SC}(T) = J_{SC}(T_0)\left(1 + \alpha\left(T - T_0\right)\right) \tag{8}$$

FIGURE 7 | J_{SC} variation in relation to interface defect density of (a) PCBM/CsSnI$_3$, (b) GO/CsSnI$_3$.
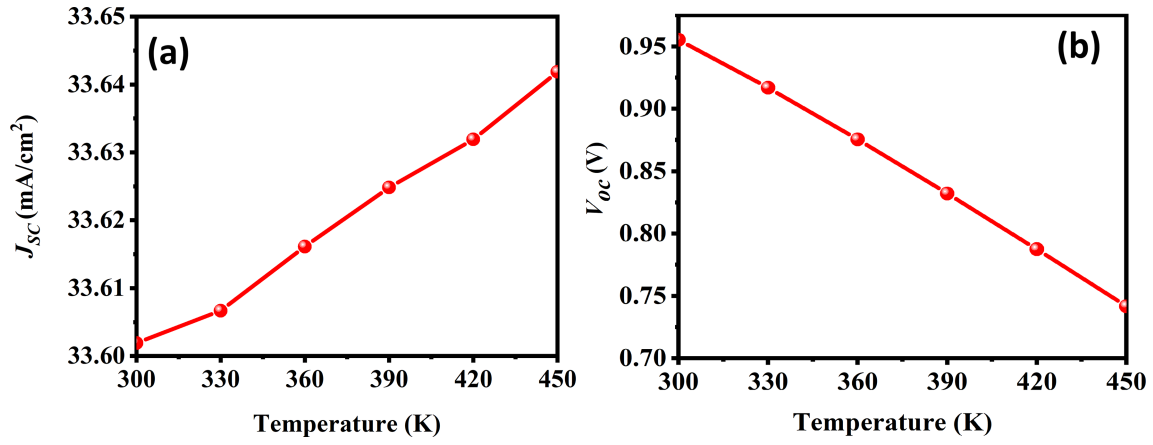
FIGURE 8 | (a) Changes in J_{SC} with temperature, (b) changes in V_{OC} with temperature.
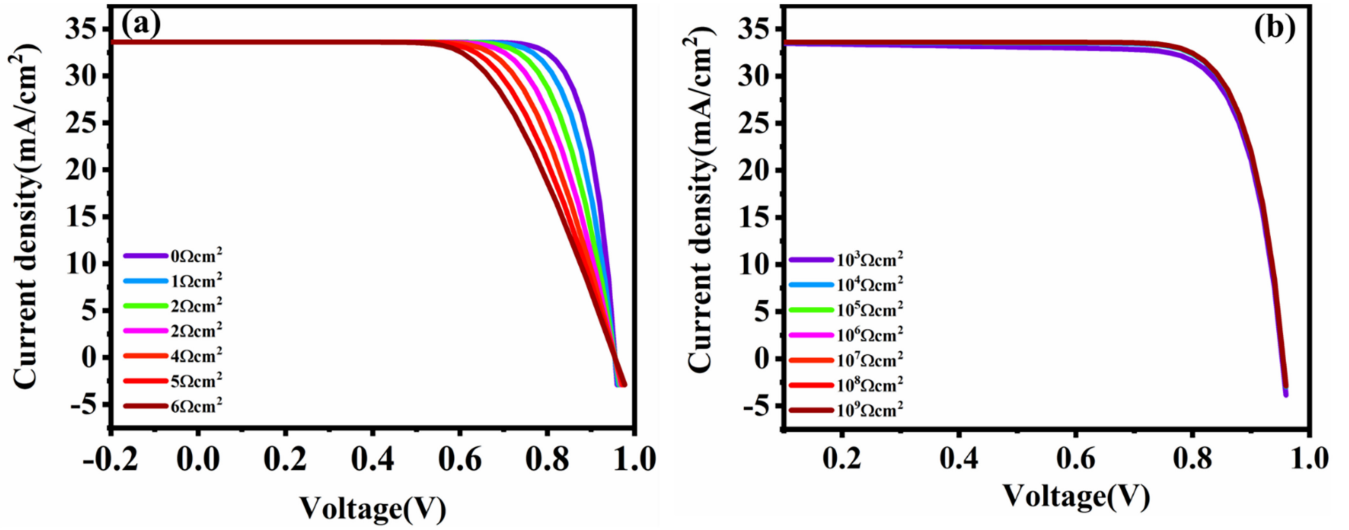

FIGURE 9 | (a) J_{SC}–voltage relationship across various series resistance (R_s) values. (b) J_{SC}–voltage relationship across different shunt resistance (R_{sh}).

where $J_{SC}(T)$ is short-circuit current density at temperature T, $J_{SC}(T_0)$ is short-circuit current density at a reference temperature T_0 and α is the temperature coefficient of J_{SC}, which depends on material properties and is typically a small positive value.

These findings stress the criticality of thermal regulation of the proposed PPD to mitigate the adverse thermal effects on charge carrier dynamics, ensuring high fidelity in performance under varying thermal conditions [39–41].

3.8 | Impact of Series and Shunt Resistance on the Device

Energy dissipation is induced by resistances. The internal resistance of a diode shows an ohmic decrease, in addition to the junction voltage drop, which pertains to the resistance present in the semiconductor material. Both the series resistance (R_s) and shunt resistance (R_{sh}) are critical component within electro-optic material that influence the electrical characteristics. Ideally, R_s should possess a value of zero, whereas R_{sh} would be infinite.

Nevertheless, in practical scenarios, R_s emerges because of the contact resistance among the layers utilized in the model, along with the resistance associated with both the front and back contact metals. Shunt resistance is predominantly affected by recombination in defect states, leading to an increase in device shunt resistance as defect states decreases. Variations in thickness and defect also affect series resistance and shunt resistance [18, 42].

Figure 9a demonstrates that an increase in series resistance leads to a reduction in J_{MPP} (current density at maximum power point). Conversely, as shown in Figure 9b, a decrease in shunt resistance results in a reduction of J_{MPP}.

3.9 | Responsivity and Detectivity of Proposed PPD

Responsivity is characterized by the ratio between photocurrent and incident-light intensity as shown in Equation (9) [43].

$$R = \frac{J_{ph}}{L_{light}} \tag{9}$$

The photocurrent, denoted as J_{ph}, is dependent on the incident-light intensity, represented by L_{light}. The relationship between R and the photodetector's external quantum efficiency (EQE), which defines how effectively photons are converted to electrons or holes, allows R to also be described as [44]

$$R = \frac{EQE \times \lambda \times q}{hc} \tag{10}$$

$$R = EQE \frac{\lambda\,(\mu m)}{1.24} \tag{11}$$

where R is used to denote responsivity, λ is utilized to represent the wavelength of light and EQE is used to denote the external quantum efficiency. In line with Equation (11), the responsivity of the device is directly influenced by the λ, resulting in a higher responsivity for longer wavelengths. The quantum efficiency of the proposed PPD, which is crucial for the determination of responsivity, is depicted in Figure 10a, and Figure 10b demonstrates the responsivity, with the peak

responsivity observed in the range of 850 to 920 nm, reaching a value of 0.68 A/W.

Specific detectivity (D^*) is considered a crucial characteristic of a photodetector, as it is used to describe the minimum level of light that a device is capable to detecting. This parameter is influenced by both the noise and responsiveness characteristics of the photodetector. The formula for D^* is expressed as [38, 40, 41]

$$D^* = \frac{R}{(2ej)^{\frac{1}{2}}} \tag{12}$$

R represents the responsivity and e represents elementary charge, whereas j denotes the dark current density in cases where the dark current is primarily influenced by shot noise. A graphical representation of device performance in relation to external bias is presented. The highest detectivity 9×10^{12} jones is observed for the proposed PPD as shown in Figure 11b, indicating a commendable performance of the photodetector.
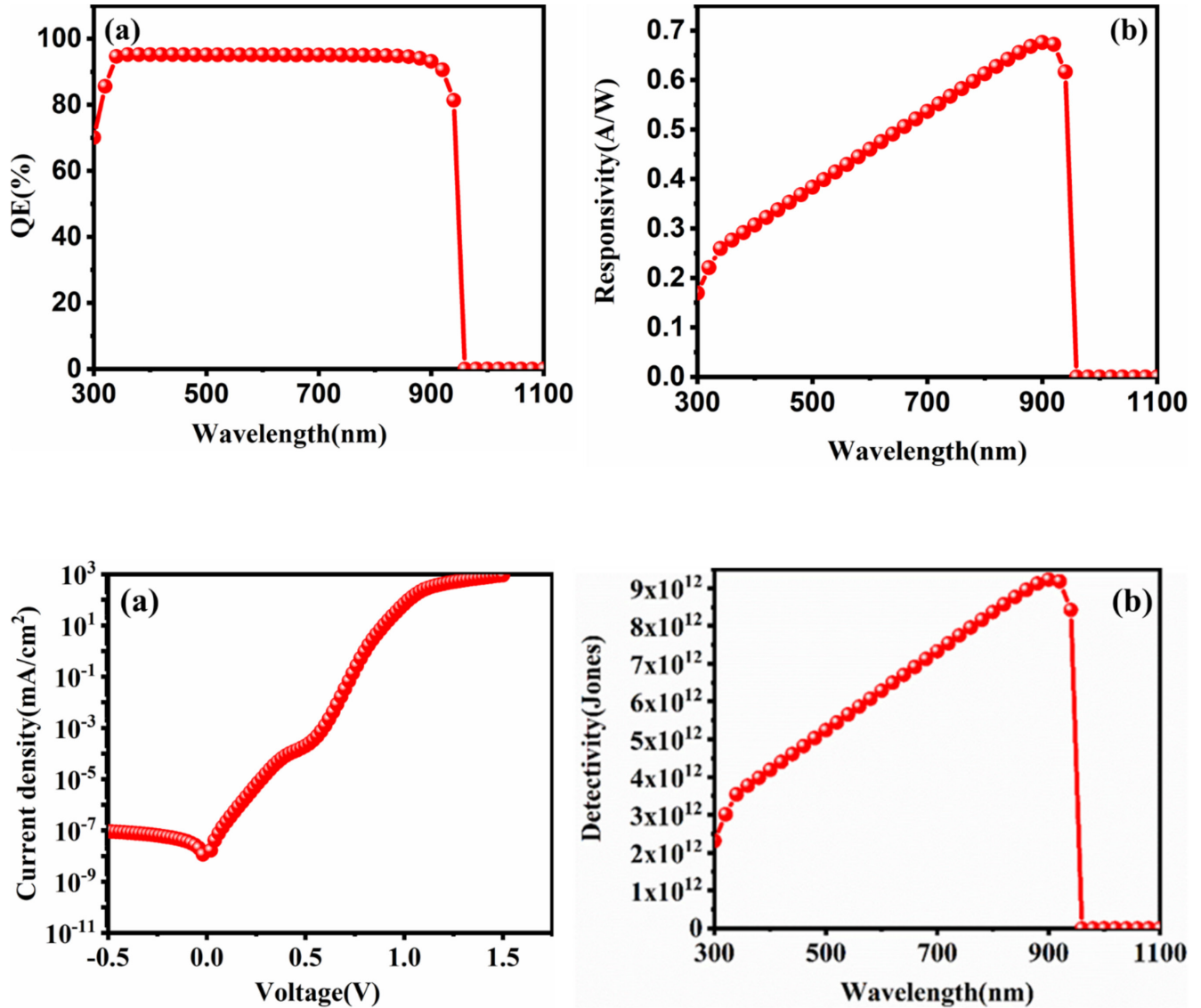

FIGURE 11 | (a) Dark current versus voltage, (b) detectivity variation across various light wavelengths.

FIGURE 10 | (a) Quantum efficiency. (b) Responsivity variation across different light wavelengths.

TABLE 2 | Comparison table.

References	R (A/W)	$D*$ (Jones)
Hybrid graphene-perovskite photodetector [45]	0.022	3.55×10^9
$Cs_3Bi_2I_9$-based photodetector WS_2/Ge [2]	0.033	1×10^{10}
Highly efficient self-powered perovskite-based photodiode [44]	0.360	2.1×10^{11}
Heterojunction-based photodetector [46]	0.63	4.3×10^{11}
GaSe/PtSe$_2$-based photodetector [47]	1.7	3.51×10^{12}
Photodetector proposed in this work	0.68	9×10^{12}

Figure 11a shows the dark current measured across a bias voltage range of −0.5 to 1.5 V. Furthermore, the proposed photodetector displayed remarkable capabilities not only in red light but also showed a better response in infrared light under consistent light intensities ranging from 850 to 920 nm.

3.10 | Comparative Analysis

Table 2 provides a comparative analysis of the responsivity (R) and detectivity ($D*$) metrics across various photodetectors, underscoring the progress in the field of perovskite-based photodetector technology. The photodetector proposed in this study demonstrates a substantial leap forward, registering a responsivity of 0.68 A/W coupled with an exceptional detectivity of 9×10^{12} Jones. This performance markedly surpasses that of similar perovskite-based devices shown in Table 2, confirming a pronounced improvement in detecting weak light signals while maintaining minimal noise interference. The elevated detectivity metric particularly indicates that the proposed photodetector stands out as a highly sensitive solution for stringent applications, leading the way in high-precision optical sensing.

4 | Conclusion

This research has successfully designed an environmentally benign and highly sensitive PPD that utilizes $CsSnI_3$ for the light-absorption layer. By integrating GO as the hole transport layer and PCBM as the ETL, the device facilitates efficient charge carrier management. The resultant photodetector boasts an exceptional responsivity of 0.68 A/W and a detectivity of 9×10^{12} Jones, demonstrating its capability to outperform conventional photodetector technologies. A meticulous analysis of the device's behaviour under varying layer thicknesses, temperatures and resistive loads has been conducted, revealing the significant impact these factors have on performance. The findings from this study are instrumental in guiding the enhancement of future photodetector designs and confirm the promise of lead-free perovskite materials in creating cost-effective, high-performing photodetection systems. The advancements made herein contribute to the evolution of next-generation photodetectors that offer unmatched sensitivity and precision, with broad implications for environmental, medical and optical technological applications.

References

1. C. Li, H. Wang, F. Wang, et al., "Ultrafast and Broadband Photodetectors Based on a Perovskite/Organic Bulk Heterojunction for Large-Dynamic-Range Imaging," *Light: Science & Applications* 9 (2020): 31, https://doi.org/10.1038/s41377-020-0264-5.

2. Z. Qi, X. Fu, T. Yang, et al., "Highly Stable Lead-Free Cs3Bi2I9 Perovskite Nanoplates for Photodetection Applications," *Nano Research* 12 (2019): 1894–1899, https://doi.org/10.1007/s12274-019-2454-0.

3. X. Hu, X. Zhang, L. Liang, et al., "High-Performance Flexible Broadband Photodetector Based on Organolead Halide Perovskite," *Advanced Functional Materials* 24 (2014): 7373–7380, https://doi.org/10.1002/adfm.201402020.

4. X. Xu, C. C. Chueh, P. Jing, et al., "High-Performance Near-IR Photodetector Using Low-Bandgap MA0.5FA0.5Pb0.5Sn0.5I3 Perovskite," *Advanced Functional Materials* 27 (2017): 1701053, https://doi.org/10.1002/adfm.201701053.

5. P. V. K. Yadav, B. Ajitha, Y. A. Kumar Reddy, and A. Sreedhar, "Recent Advances in Development of Nanostructured Photodetectors From Ultraviolet to Infrared Region: A Review," *Chemosphere* 279 (2021): 130473, https://doi.org/10.1016/j.chemosphere.2021.130473.

6. L. Li, Y. Huang, J. Peng, Y. Cao, and X. Peng, "Highly Responsive Organic Near-Infrared Photodetectors Based on a Porphyrin Small Molecule," *Journal of Materials Chemistry C* 2 (2014): 1372–1375, https://doi.org/10.1039/c3tc32171a.

7. L. Shen, Y. Zhang, Y. Bai, X. Zheng, Q. Wang, and J. Huang, "A Filterless, Visible-Blind, Narrow-Band, and Near-Infrared Photodetector With a Gain," *Nanoscale* 8 (2016): 12990–12997, https://doi.org/10.1039/c6nr02902g.

8. L. Shen, Y. Fang, H. Wei, Y. Yuan, and J. Huang, "A Highly Sensitive Narrowband Nanocomposite Photodetector With Gain," *Advanced Materials* 28 (2016): 2043–2048, https://doi.org/10.1002/adma.201503774.

9. A. Rogalski, J. Antoszewski, and L. Faraone, "Third-Generation Infrared Photodetector Arrays," *Journal of Applied Physics* 105 (2009): 091101, https://doi.org/10.1063/1.3099572.

10. S. Yadav, P. Lohia, and A. Sahu, "Enhanced Performance of Double Perovskite Solar Cell Using WO₃ as an Electron Transport Material," *Journal of Optics (India)* 52 (2023): 776–782, https://doi.org/10.1007/s12596-022-01035-3.

11. S. Yadav, P. Lohia, and A. Sahu, "Impact of Generation Recombination Rate in STO-Enabled (FA)2BiCuI6-Based Double Perovskite Solar

Cell Without HTL," *Journal of Optics (India)* 53 (2023): 3604–3616, https://doi.org/10.1007/s12596-023-01535-w.

12. Y. Fang, Q. Dong, Y. Shao, Y. Yuan, and J. Huang, "Highly Narrow-band Perovskite Single-Crystal Photodetectors Enabled by Surface-Charge Recombination," *Nature Photonics* 9 (2015): 679–686, https://doi.org/10.1038/nphoton.2015.156.

13. L. Dou, Y. M. Yang, J. You, et al., "Solution-Processed Hybrid Perovskite Photodetectors With High Detectivity," *Nature Communications* 5 (2014): 5404, https://doi.org/10.1038/ncomms6404.

14. G. Xing, N. Mathews, S. Sun, et al., "Long-Range Balanced Electron- and Hole-Transport Lengths in Organic-Inorganic CH3NH3PbI3," *Science* 342, no. 2013 (1979): 344–347, https://doi.org/10.1126/science.1243167.

15. I. Chung, B. Lee, J. He, R. P. H. Chang, and M. G. Kanatzidis, "All-Solid-State Dye-Sensitized Solar Cells With High Efficiency," *Nature* 485 (2012): 486–489, https://doi.org/10.1038/nature11067.

16. J. Jiang, C. K. Onwudinanti, R. A. Hatton, P. A. Bobbert, and S. Tao, "Stabilizing Lead-Free All-Inorganic Tin Halide Perovskites by Ion Exchange," *Journal of Physical Chemistry C* 122 (2018): 17660–17667, https://doi.org/10.1021/acs.jpcc.8b04013.

17. I. Chung, J. H. Song, J. Im, et al., "CsSnI 3: Semiconductor or Metal? High Electrical Conductivity and Strong Near-Infrared Photoluminescence From a Single Material. High Hole Mobility and Phase-Transitions," *Journal of the American Chemical Society* 134 (2012): 8579–8587, https://doi.org/10.1021/ja301539s.

18. M. F. Wahid, M. S. Rahman, N. Ahmed, et al., "Performance Enhancement of Lead-Free CsSnI$_3$ Perovskite Solar Cell: Design and Simulation With Different Electron Transport Layers," *IEEE Access* 12 (2024): 8296–8312, https://doi.org/10.1109/ACCESS.2024.3352444.

19. L. Zhang, L. Mei, K. Wang, et al., "Advances in the Application of Perovskite Materials," *Nano-Micro Letters* 15 (2023): 177, https://doi.org/10.1007/s40820-023-01140-3.

20. G. Chen, T. X. Han, Z. He, R. Kays, and T. Forrester, "Deep Convolutional Neural Network Based Species Recognition for Wild Animal Monitoring," in *2014 IEEE International Conference on Image Processing (ICIP)*, (Paris, France: IEEE, 2014): 858–862. https://doi.org/10.1109/ICIP.2014.7025172.

21. Z. Li, J. Li, D. Ding, et al., "Direct Observation of Perovskite Photodetector Performance Enhancement by Atomically Thin Interface Engineering," *ACS Applied Materials & Interfaces* 10 (2018): 36493–36504, https://doi.org/10.1021/acsami.8b10971.

22. H. Zhou, J. Mei, M. Xue, Z. Song, and H. Wang, "High-Stability, Self-Powered Perovskite Photodetector Based on a CH3NH3PbI3/GaN Heterojunction With C60 as an Electron Transport Layer," *Journal of Physical Chemistry C* 121 (2017): 21541–21545, https://doi.org/10.1021/acs.jpcc.7b07536.

23. J. Pan, L. Mao, Z. Gao, et al., "Highly Stable and Sensitive Solar-Blind Photodetectors Based on CsCu2I3 Perovskites," *IEEE Electron Device Letters* 44 (2023): 1660–1663, https://doi.org/10.1109/LED.2023.3307413.

24. Y. Wang, J. Tu, T. Li, C. Tao, X. Deng, and Z. Li, "Convenient Preparation of CsSnI$_3$ Quantum Dots, Excellent Stability, and the Highest Performance of Lead-Free Inorganic Perovskite Solar Cells so Far," *Journal of Materials Chemistry A* 7 (2019): 7683–7690, https://doi.org/10.1039/c8ta10901j.

25. M. Mostefaoui, H. Mazari, S. Khelifi, A. Bouraiou, and R. Dabou, "Simulation of High Efficiency CIGS Solar Cells With SCAPS-1D Software," *Energy Procedia* 74 (2015): 736–744, https://doi.org/10.1016/j.egypro.2015.07.809.

26. M. S. Shamna, K. S. Nithya, and K. S. Sudheer, "Simulation and Optimization of CH3NH3SnI3 Based Inverted Perovskite Solar Cell With NiO as Hole Transport Material," *Materials Today Proceedings* 33 (2019): 1246–1251, https://doi.org/10.1016/j.matpr.2020.03.488.

27. A. K. Chaudhary, S. Verma, and R. K. Chauhan, "Design of a Low-Cost, Environment Friendly Perovskite Solar Cell With Synergic Effect of Graphene Oxide-Based HTL and CH3NH3GeI3 as ETL," *Engineering Research Express* 5 (2023): 035039, https://doi.org/10.1088/2631-8695/acee45.

28. A. K. Chaudhary, S. Verma, and R. K. Chauhan, "Thermal and Power Performance Optimization of Cost-Effective Solar Cells Using Eco-Friendly Perovskite Materials," *Physica Scripta* 99 (2024): 025512, https://doi.org/10.1088/1402-4896/ad196e.

29. M. Azadinia, M. Ameri, R. T. Ghahrizjani, and M. Fathollahi, "Maximizing the Performance of Single and Multijunction MA and Lead-Free Perovskite Solar Cell," *Materials Today Energy* 20 (2021): 100647, https://doi.org/10.1016/j.mtener.2021.100647.

30. X. Lin, D. Cui, X. Luo, et al., "Efficiency Progress of Inverted Perovskite Solar Cells, Energy," *Environmental Sciences* 13 (2020): 3823–3847, https://doi.org/10.1039/d0ee02017f.

31. A. Roy and A. Majumdar, "Numerical Optimization of Cu$_2$O as HTM in Lead-Free Perovskite Solar Cells: A Study to Improve Device Efficiency," *Journal of Electronic Materials* 52 (2023): 2020–2033, https://doi.org/10.1007/s11664-022-10181-0.

32. M. K. Hossain, M. S. Uddin, G. F. I. Toki, et al., "Achieving Above 24% Efficiency With Non-Toxic CsSnI$_3$ Perovskite Solar Cells by Harnessing the Potential of the Absorber and Charge Transport Layers," *RSC Advances* 13 (2023): 23514–23537, https://doi.org/10.1039/d3ra02910g.

33. N. J. Valeti, K. Prakash, M. K. Singha, and A. Kumar, "Numerical Investigation of CuSbS$_2$ Thin Film Solar Cell Using SCAPS-1D: Enhancement of Efficiency on Experimental Films by Defect Studies," *Materials Research Express* 11 (2024): 045506, https://doi.org/10.1088/2053-1591/ad371a.

34. Y. M. Lee, I. Maeng, J. Park, et al., "Comprehensive Understanding and Controlling the Defect Structures: An Effective Approach for Organic-Inorganic Hybrid Perovskite-Based Solar-Cell Application," *Frontiers in Energy Research* 6 (2018): 128, https://doi.org/10.3389/fenrg.2018.00128.

35. W. Abdelaziz, A. Shaker, M. Abouelatta, and A. Zekry, "Possible Efficiency Boosting of Non-Fullerene Acceptor Solar Cell Using Device Simulation," *Optical Materials* 91 (2019): 239–245, https://doi.org/10.1016/j.optmat.2019.03.023.

36. K. Deepthi Jayan and V. Sebastian, "Comprehensive Device Modelling and Performance Analysis of MASnI$_3$ Based Perovskite Solar Cells With Diverse ETM, HTM and Back Metal Contacts," *Solar Energy* 217 (2021): 40–48, https://doi.org/10.1016/j.solener.2021.01.058.

37. A. K. Chaudhary, S. Verma, and R. K. Chauhan, "MASnI$_3$-Based Perovskite Solar Cell Utilizing Oxygen-Free Charge Transport Layers to Alleviate Sn Oxidation for Stability: A Comprehensive Investigation," *Journal of Renewable and Sustainable Energy* 16 (2024): 053702, https://doi.org/10.1063/5.0220018.

38. P. Singh and N. M. Ravindra, "Temperature Dependence of Solar Cell Performance—An Analysis," *Solar Energy Materials and Solar Cells* 101 (2012): 36–45, https://doi.org/10.1016/j.solmat.2012.02.019.

39. A. D. Dhassa, E. Natarajana, and P. Lakshmi, "An Investigation of Temperature Effects on Solar Photovoltaic Cells and Modules," *International Journal of Engineering, Transactions B: Applications* 27 (2014): 1713–1722, https://doi.org/10.5829/idosi.ije.2014.27.11b.09.

40. R. L. Yang, G. M. Tiepolo, É. A. Tonolo, J. Urbanetz, and M. B. de Souza, "Photovoltaic Cell Temperature Estimation for a Grid-Connect Photovoltaic Systems in Curitiba," *Brazilian Archives of Biology and Technology* 62 (2019): 1–9, https://doi.org/10.1590/1678-4324-SMART-2019190016.

41. S. Datta, M. M. Hossain, S. Nuzhat, A. Debnath, and H. Huq, "Performance Study of an Optimized Lead-Free $Cs_3Sb_2I_9$-Based Perovskite Solar Cell Using SCAPS-1D," in *2022 IEEE Green Technologies Conference (GreenTech)*, (Houston, TX: IEEE, 2022): 80–85, https://doi.org/10.1109/GreenTech52845.2022.9772038.

42. M. K. Hossain, S. Bhattarai, A. A. Arnab, et al., "Harnessing the Potential of $CsPbBr_3$-Based Perovskite Solar Cells Using Efficient Charge Transport Materials and Global Optimization," *RSC Advances* 13 (2023): 21044–21062, https://doi.org/10.1039/d3ra02485g.

43. H. Wang and D. H. Kim, "Perovskite-Based Photodetectors: Materials and Devices," *Chemical Society Reviews* 46 (2017): 5204–5236, https://doi.org/10.1039/c6cs00896h.

44. A. M. Afzal, I. G. Bae, Y. Aggarwal, et al., "Highly Efficient Self-Powered Perovskite Photodiode With an Electron-Blocking Hole-Transport NiO_x Layer," *Scientific Reports* 11 (2021): 169, https://doi.org/10.1038/s41598-020-80640-3.

45. Z. Chen, Z. Kang, C. Rao, et al., "Improving Performance of Hybrid Graphene–Perovskite Photodetector by a Scratch Channel," *Advanced Electronic Materials* 5 (2019): 1900168, https://doi.org/10.1002/aelm.201900168.

46. D. Wu, J. Guo, C. Wang, et al., "Ultrabroadband and High-Detectivity Photodetector Based on WS_2/Ge Heterojunction Through Defect Engineering and Interface Passivation," *ACS Nano* 15 (2021): 10119–10129, https://doi.org/10.1021/acsnano.1c02007.

47. K. Gong, L. Li, W. Yu, et al., "High Detectivity and Fast Response Avalanche Photodetector Based on GaSe/PtSe2 p–n Junction," *Materials and Design* 228 (2023): 111848, https://doi.org/10.1016/j.matdes.2023.111848.